

pubs.acs.org/JPCL Letter

Enhancing Stability of Surface Au under Oxidizing Conditions through Reduced Bulk Au Content

Jianyu Wang, Xiaobo Chen, Chaoran Li, Yaguang Zhu, Jing Li, Shiyao Shan, Yupeng Wu, Adrian Hunt, Iradwikanari Waluyo, J. Anibal Boscoboinik, Xiao Tong, Chuan-Jian Zhong, and Guangwen Zhou*



Cite This: J. Phys. Chem. Lett. 2024, 15, 10583-10591



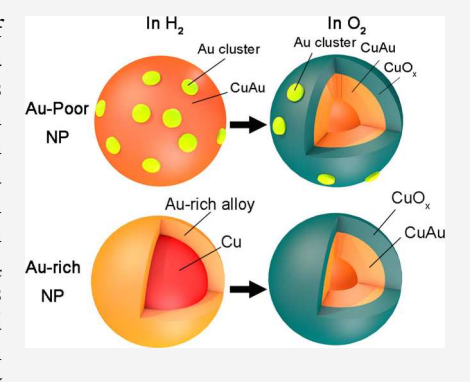
ACCESS I

III Metrics & More

Article Recommendations

s Supporting Information

ABSTRACT: Contrary to the common assumption that a higher bulk content of precious metals facilitates the preservation of more surface noble metal by serving as a reservoir for surface enrichment, we demonstrate that a lower bulk content of Au results in a more stable arrangement of Au atoms at the surface of Cu–Au nanoparticles when exposed to an O_2 atmosphere. Using ambient pressure X-ray photoelectron spectroscopy, we investigate the surface segregation and oxidation behavior of Cu–Au nanoparticles across various compositions. Our results reveal that in Au-rich nanoparticles exposed to an H_2 atmosphere, surface segregation prompts the formation of a continuous Au-enriched shell, which subsequently oxidizes into a complete CuO_x shell upon transitioning to an O_2 atmosphere. Conversely, in Au-poor nanoparticles during H_2 treatment, segregation results in the emergence of Au clusters embedded within the surface layer, persisting upon exposure to O_2 . This unexpected phenomenon shows that reducing the bulk content of precious metals can enhance the surface stability



of noble atoms under oxidizing conditions, as further demonstrated by comparing the catalytic performance of Cu–Au nanoparticles with varying Au bulk contents in CO oxidation.

lloying is a widely adopted approach for fine-tuning A catalytic properties, offering advantages over individual pure metals.^{1–3} Among various bimetallic systems, Cu–Au alloys have gained considerable attention for their synergistic effects in a range of industrially important reactions, including partial oxidation of methanol, selective hydrogenation, and CO oxidation.⁶ The performance of Cu-Au catalysts hinges significantly on their surface structure and composition, which govern the active sites for reactant and product molecule adsorption, reaction, and desorption. 5-7 The bulk of the catalyst, on the other hand, may serve as a reservoir of catalytically active species or as a support for the active surface sites, contributing to the overall stability and durability of the catalyst. Maximizing surface concentration and stability of Au while minimizing bulk precious metal content is highly desirable for cost-effectiveness. Surface segregation phenomena in reducing atmospheres like H₂ enrich Au at the surface.^{8–10} However, the presence of O₂ during catalytic oxidation may induce surface Cu oxide formation, potentially burying the catalytically active Au, and leading to catalyst deactivation.¹¹ Thus, preserving surface Au during O2 exposure is crucial for maintaining catalytic functionality.

The situation becomes even more challenging for nanoparticle (NP) catalysts, where the nanoscale size effect can play a crucial role in altering the surface segregation and oxidation behavior of nanoalloys. This is because the significantly increased surface-to-volume ratio and altered surface energetics open up a variety of additional freedoms and driving forces to initiate a surface segregation process. Moreover, the increased surface area of NPs also enhances their susceptibility to oxidation, making it more challenging to maintain the noble metal on the surface in an oxidizing atmosphere. Therefore, it is commonly assumed that a higher bulk content of precious metals facilitates the preservation of more surface noble metal by serving as a reservoir for surface enrichment. Contrary to this conventional notion, herein we demonstrate that a lower bulk content of Au results in a more stable arrangement of Au atoms at the surface of Cu—Au NPs when exposed to an O₂ atmosphere. This unexpected outcome highlights the nuanced relationship between bulk composition and surface stability, suggesting that reducing the bulk Au content can enhance the surface stability of Au atoms under oxidizing conditions.

Our in situ measurements utilize synchrotron-based ambient-pressure X-ray photoelectron spectroscopy (AP-XPS) to comparatively monitor the dynamic evolution of surface compositions of $Cu_{75}Cu_{25}$ and $Cu_{90}Au_{10}$ NPs under both H_2 and O_2 atmospheres. Figure 1(a) shows the spectra

Received: July 23, 2024
Revised: September 19, 2024
Accepted: October 9, 2024
Published: October 15, 2024





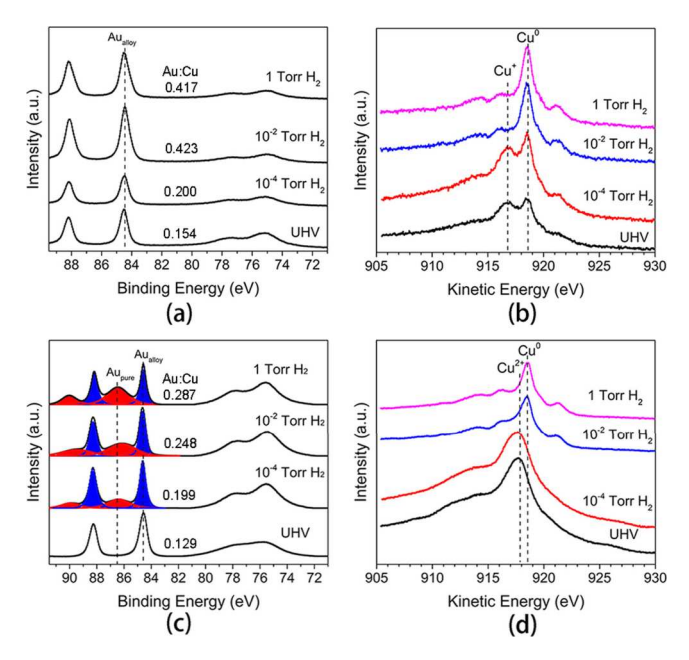


Figure 1. Evolution of Au 4f, Cu 3p, and Cu LMM spectra acquired during the $\rm H_2$ annealing of (a, b) $\rm Cu_{75}Au_{25}$ and (c, d) $\rm Cu_{90}Au_{10}$ NPs at 400 °C. Spectra for Au 4f and Cu 3p were obtained using an incident photon energy of 650 eV, while spectra for Cu LMM were obtained using an incident photon energy of 1150 eV. The annealing process involves a stepwise increase in $\rm H_2$ pressure from UHV to \sim 1 Torr.

obtained from the Au 4f and Cu 3p regions during the annealing of Cu₇₅Au₂₅ NPs at 400 °C, from ultrahigh vacuum (UHV) to a stepwise increase of H₂ pressure to 1 Torr. The binding energies (BEs) are corrected for substrate charging using the C 1s peak from the HOPG support at 284.8 eV and Cu $2p_{3/2}$ peak at BE = 932.6 eV as references.¹⁴ The Au 4f region consists of two components corresponding to Au 4f_{5/2} and Au $4f_{7/2}$, respectively. The Au $4f_{7/2}$, centered at BE = 84.5 eV, indicates an alloy state of Au in the Cu75Au25 NPs with a higher BE than pure Au at 84 eV. 10,111 The alloy Au state predominates under UHV and during H2 annealing. Notably, its peak intensity significantly increases upon raising the H₂ pressure to 1×10^{-2} Torr, indicating surface segregation of Au and subsequent enrichment of alloy Au at the surface. However, increasing the H₂ pressure to 1 Torr results in the attenuation of the overall intensity of the XPS signals due to the scattering of photoelectrons by the presence of a significant amount of gas molecules within the chamber.

The intensity evolution of the coordinated Au 4f and Cu 3p spectra in Figure 1(a) can be quantified to monitor changes in the Au composition during H_2 exposure using the area ratio of Au 4f to Cu 3p, normalized by their Scofield scattering factors ($\sigma_{\text{Cu 3p}} = 2.478$, $\sigma_{\text{Au 4f}} = 17.12$). Initially, under UHV conditions, the Au/Cu area ratio is 0.154, which is lower than the bulk composition ratio of 0.33, suggesting the presence of surface CuO_x . As H_2 pressure increases, the Au/Cu area ratio increases and reaches a saturation value of 0.42 at 0.1 and 1 Torr H_2 . This indicates that the surface CuO_x is fully reduced at 0.1 Torr H_2 . The Cu $3p_{3/2}$ peak, located at BE = 75.1 eV, is characteristic of Cu and Cu_2O . Solution the Cu 3p spectra show no significant core-level shifts during H_2 annealing due to the close binding energy between Cu and Cu_2O in the Cu 3p region, the intensity of the Cu 3p region decreases with continued H_2 annealing due to surface

segregation of Au, which results in the attenuation of the Cu 3p signal. Figure 1(b) illustrates the coordinated Cu LMM Auger spectra, confirming that the as-prepared Cu₇₅Au₂₅ NPs are partially oxidized, with initial chemical states comprising a mixture of Cu⁰ (918.6 eV) and Cu⁺ (916.9 eV). Additionally, the Auger spectra reveal that the Cu⁺ is entirely reduced to metallic Cu⁰ during H₂ annealing at 1 \times 10⁻² Torr H₂. By combining the evolution of the Au 4f, Cu 3p, and Cu LMM, it can be concluded that H₂ annealing of the Cu₇₅Au₂₅ NPs results in the complete reduction of native Cu oxide, leading to a significant surface enrichment of Au.

Figure 1(c) depicts the evolution of Au 4f and Cu 3p spectra during the H₂ annealing of Cu₉₀Au₁₀ NPs at 400 °C with a stepwise increase in H₂ pressure from UHV to 1 Torr. Initially, under UHV annealing, the Au 4f is predominantly comprised of the alloy state at 84.5 eV. Upon switching to H₂ annealing, a new peak emerges at BE = 86.5 eV, with its intensity growing stronger as the H₂ pressure increases. This new peak exhibits considerable broadening with a full width at half-maximum (fwhm) of 2 eV, in contrast to the alloy Au peak at 84.5 eV with a fwhm of 0.9 eV. Furthermore, Figure 1(c) demonstrates the absence of the pure Au peak at BE = 84 eV during H₂ annealing. The emergence of this new peak at BE = 86.5 eV is attributed to the formation of extremely small Au clusters, as will be discussed later by DFT calculation. The intensity evolution of the Au 4f and Cu 3p spectra for Cu₉₀Au₁₀ NPs is summarized in Figure 1(c). Similar to the behavior observed in Cu₇₅Au₂₅ NPs, the Au/Cu area ratio rises with increasing H₂ pressure, surpassing the bulk composition and resulting in the development of an Au-rich surface. The notable intensity in the Cu 3p region under UHV annealing indicates the presence of Cu oxides for the Cu₉₀Au₁₀ sample, with the most intense peak at BE = 76.4 eV corresponding to CuO. The H₂ annealing results in the reduction of CuO to Cu, as indicated with the shift of the most intense peak to BE = 75.1 eV. This reduction is further confirmed by the coordinated Cu LMM spectra shown in Figure 1(d), which illustrate the complete reduction of Cu oxides (917.9 eV) to Cu⁰ (918.6 eV) at 1 Torr H₂. It is worth noting that the emergence of the new Au peak at 86.5 eV begins at low H_2 pressure of 1×10^{-4} Torr, where the surface oxide is not yet fully reduced.

The discrepancy between the Cu₉₀Au₁₀ and Cu₇₅Au₂₅ samples is further supported by in situ AP-XPS measurements on Cu, Cu₅₀Au₅₀ and Cu₉₅Au₅ NPs under similar reducing conditions, as shown in Supplementary Figure S1. Specifically, the Au 4f region of the Cu NP sample shows only the background signals without any detectable peaks, despite extended H₂ annealing. This confirms that the new peak at BE = 86.5 eV observed in the Cu₉₀Au₁₀ sample is not related to Cu. Moreover, the data for Cu₉₅Au₅ and Cu₅₀Au₅₀ samples reveal a similar trend to that observed between the Cu75Au25 and Cu₉₀Au₁₀ samples, with a prominent new peak emerging in the Cu₉₅Au₅ sample due to the formation of very small Au clusters. This difference indicates that Au surface segregation in Au-poor NPs (such as Cu₉₀Au₁₀ and Cu₉₅Au₅) leads to the formation of Au clusters in the surface region, while Au-rich NPs (like Cu₇₅Au₂₅ and Cu₅₀Au₅₀) tend to develop an Au-rich alloy shell under H₂ annealing.

Figure 2(a) displays the evolution of Au 4f and Cu 3p spectra of H_2 -treated $Cu_{75}Au_{25}$ NPs at 400 °C after switching from UHV to O_2 exposure. Compared to the UHV annealing, exposure to O_2 at $pO_2 = 1 \times 10^{-2}$ Torr for 10 min leads to a slight increase in the intensity of the Cu 3p region with respect

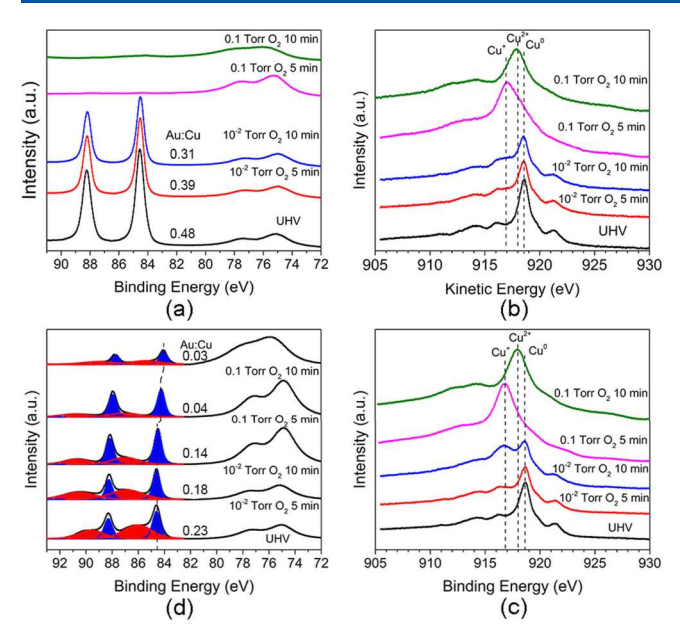


Figure 2. Time evolution of (a, c) Au 4f and Cu 3p spectra obtained with an incident photon energy of 650 eV and (b, d) Cu LMM spectra obtained with an incident photon energy of 1150 eV, for H₂-treated Cu₇₅Au₂₅ and Cu₉₀Au₁₀ NPs at 400 °C. The process progresses from UHV to 1×10^{-2} Torr O₂, and subsequently to 0.1 Torr O₂.

to the Au 4f region, indicating minor Cu oxidation. Increasing pO₂ to 0.1 Torr results in the complete absence of the Au 4f intensity and a stronger intensity in the Cu 3p region, indicating the formation of a thick surface overlayer of Cu oxide. Figure 2(b) illustrates the correlated Cu LMM Auger spectra, demonstrating that Cu is partially oxidized to Cu₂O, as evidenced by the shoulder at BE = 916.9 eV, at 400 °C for 10 min at $pO_2 = 1 \times 10^{-2}$ Torr, and then completely oxidized to Cu₂O for 5 min and CuO for 10 min at $pO_2 = 0.1$ Torr. The combined measurements of Au 4f, Cu 3p and Cu LMM confirm that the Cu₇₅Au₂₅ NPs are initially oxidized to a Cu₂O@CuAu shell—core configuration at $pO_2 = 1 \times 10^{-2}$ Torr and subsequently to the CuO@CuAu shell—core structure at $pO_2 = 0.1$ Torr, where the thick CuO shell completely attenuates the photoelectrons from the CuAu core.

Figure 2(c) presents the spectra acquired from the Au 4f and Cu 3p regions during the exposure of $\text{Cu}_{90}\text{Au}_{10}$ NPs at 400 $^{\circ}\text{C}$, progressing from UHV to $pO_2 = 1 \times 10^{-2}$ Torr, and subsequently to $pO_2 = 0.1$ Torr. Initially, under UHV, a shoulder at BE = 86 eV is observable, corresponding to the small Au clusters formed during H2 annealing (as depicted in Figure 1(c)). Upon switching to $pO_2 = 1 \times 10^{-2}$ Torr, the peak of small Au clusters diminishes alongside a weakened intensity of the alloy Au peak, shifting to BE = 87 eV due to changes to a smaller cluster size. This size dependence of the BE is reported by XPS experiments, ^{17–23} and we will discuss it using DFT modeling later. This trend persists at the higher pO₂ of 0.1 Torr, with a substantial increase in intensity in the Cu 3p region and the shift of the most intense peak to BE = 76.4 eV, indicating significant CuO growth that completely attenuates the photoelectrons from the core region. However, the Au 4f region still exhibits appreciable intensity, with the Au 4f_{7/2} BE shifting to 84 eV, indicating the presence of pure Au in the surface region. The emergence of the peak at BE = 84eV associated with large Au clusters and the BE shift from 87

to 85 eV for the small Au clusters suggests the aggregation of surface Au, leading to an increase in the size of Au clusters.

Figure 2(d) illustrates the coordinated Cu LMM spectra, showing that the Cu LMM peak position of the Cu₉₀Au₁₀ NPs prior to switching to O2 is located at 918.6 eV, characteristic of metallic Cu. Upon switching to $pO_2 = 1 \times 10^{-2}$ Torr for 10 min, the Cu LMM of the Cu₉₀Au₁₀ exhibits a prominent peak at a lower kinetic energy of 916.9 eV, corresponding to Cu⁺ in $Cu_2O.^{14}$ In contrast, the $Cu_{75}Au_{25}$ sample under $pO_2 = 1 \times 10^{-14}$ 10⁻² Torr for 10 min remains predominantly as metallic Cu⁰, with a much weaker shoulder at the kinetic energy of the Cu1+ peak (Figure 2(b)). This disparity in the Cu LMM spectral shapes indicates that the Cu₉₀Au₁₀ NPs are more readily oxidized into Cu₂O compared to Cu₇₅Au₂₅ NPs. Figure 2(d) further shows that the NPs are completely oxidized to Cu₂O for 5 min and eventually to CuO for 10 min without any detectable metallic Cu at $pO_2 = 0.1$ Torr, confirming formation of a thicker CuO overlayer on the NPs. The combined Au 4f, Cu 3p, and Cu LMM spectra depicted above demonstrate that Cu₉₀Au₁₀ NPs are oxidized into a CuO/Au@CuAu shell—core structure, where the shell consists of Au clusters embedded in the CuO shell. This contrasts with the oxidation of Cu₇₅Au₂₅ NPs under the same O₂ condition, resulting in a complete CuO shell despite their lower Cu concentration compared to Cu₉₀Au₁₀ NPs.

The intensity evolution of the coordinated Au 4f and Cu 3p spectra in Figures 2(a, c) can be quantified to track the Au:Cu composition changes during O2 exposure. Following H2 treatment, the Au:Cu ratios for Cu₇₅Au₂₅ and Cu₉₀Au₁₀ NPs are 0.48 and 0.23, respectively, exceeding the bulk Au/Cu compositions of the as-prepared NPs due to Au segregation to the pristine surfaces during H₂ annealing. For Cu₇₅Au₂₅ NPs, the Au/Cu ratio decreases to ~0.39 and ~0.31 during Cu₂O formation under pO₂ = 1×10^{-2} Torr for 5 and 10 min, respectively, and then diminishes to 0 during CuO formation under pO₂ = 0.1 Torr for 5 min. Conversely, for $Cu_{90}Au_{10}$ NPs, the Au/Cu ratio decreases to ~0.18 and ~0.14 during Cu₂O formation at $pO_2 = 1 \times 10^{-2}$ Torr for 5 and 10 min, respectively, and then drops to ~0.04 during CuO formation at $pO_2 = 0.1$ Torr for 5 min. Even after 10 min of exposure to $pO_2 = 0.1$ Torr, the Au 4f signal remains visible with an Au/Cu ratio of ~ 0.03 (Figure 2(c)).

The combined XPS and AES measurements presented above reveal a surprising contrast in the dynamic oxidation behavior between Au-rich NPs (Cu75Au25) and Au-poor NPs (Cu₉₀Au₁₀) when exposed to a similar O₂ atmosphere. Specifically, the Au-rich NPs undergo oxidation, forming a complete CuO shell on the CuAu core, whereas the Au-poor NPs are oxidized to yield a partial CuO/Au@CuAu shell-core structure, with residual Au clusters embedded in the CuO shell. This discrepancy is further supported by in situ XPS measurements performed with Cu₅₀Au₅₀ and Cu₉₅Au₅ NPs under similar oxidizing conditions (Supplementary Figure S2). Initially, this difference might seem counterintuitive, as the higher Cu content in Au-poor NPs would suggest that they would oxidize more readily to form a complete CuO shell. To reveal this discrepancy from intuitive expectations, we examine the differences in the surface compositions and configurations of pristine NPs following H2 annealing. As illustrated in Figure 1(c) and Figure 2(c), the evolution of Au 4f spectra during H_2 annealing shows the emergence of an Au state in the Au-poor NPs, with BEs varying from 87 to 85 eV. This distinct state, differing from alloy Au or pure Au, likely plays a pivotal role in driving the difference in the stability of surface Au of Au-rich and Au-poor NPs in an O_2 atmosphere. To elucidate the nature of the observed Au in Au-poor NPs, we consider size-dependent core-level BE shifts. Previous experimental and calculational studies have demonstrated that the BE of Au 4f increases with reduction in cluster size. The Au state observed in Figure 1 exhibits higher BEs than those for pure Au (BE = 84 eV) and alloy Au (84.5 eV). Consequently, it is attributed to the presence of Au clusters formed via the aggregation of surface-segregated Au atoms, with the varied BEs induced by dynamic variations in cluster sizes during H_2 annealing.

To further elucidate the origin of the BE shift associated with the new Au phase, we calculate the Au 4f core-level shifts from bulk Au and nanoclusters of Au atoms using Kohn–Sham eigenvalues. These calculations are based on cluster size, without considering the effect of cluster shapes, which may not be well developed for the surface-segregated Au during the H_2 treatment. Figure 3(a) illustrates the comparison between Au

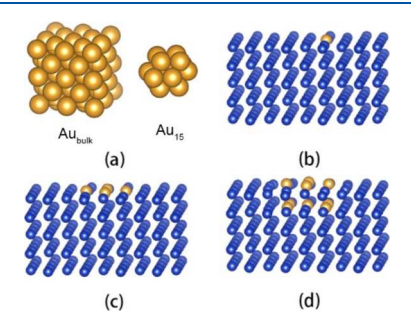


Figure 3. DFT modeling of core-level shift of Au clusters. (a) Optimized structures of bulk Au and a free-standing Au_{15} cluster; (b-d) Optimized structures of Au_1 , Au_4 , and Au_9 clusters embedded in the Cu surface.

bulk and a fully relaxed Au₁₅ cluster (consisting of 15 Au atoms) cut from bulk fcc Au. The Au₁₅ cluster periodically repeats itself in a supercell geometry, with at least a 34 Å vacuum gap between successive cells. The corner sites of Au₁₅, characterized by low coordination, exhibit a core-level shift approximately +0.42 eV higher than that of bulk Au. Similarly, the Au atom at the center of the Au₁₅ cluster shows a core-level shift of +0.24 eV compared to bulk Au. Furthermore, the average Au-Au bond distance is 2.76 Å for the Au₁₅ cluster, which is smaller than the 2.95 Å bond length in bulk Au. This finding is in good accordance with previous studies showing shorter Au-Au bond lengths in small Au clusters.^{27,33} The shorter Au-Au bond length corresponds to lattice strain, which is also found to significantly contribute to the core-level shift.³³ Therefore, we also calculate the core-levels of two bulk Au models with Au-Au bond lengths of 2.95 and 2.76 Å, respectively, revealing that the model with the shorter Au-Au bond length yields a higher BE by +0.63 eV. Consequently, the observed higher BEs for the Au clusters are attributed to their extremely small sizes, consisting of several Au atoms and embedded in the surface layer, where the larger lattice constant of Au than the surrounding Cu matrix results in compressive strains in the Au clusters. This is further corroborated by our DFT calculations, showing the core-level shifts by +0.65 eV, + 0.59 eV, and +0.3 eV for Au₁, Au₄, and Au₉ clusters embedded in the Cu surface, respectively (Figures 3(b-d)).

By contrast, the Au 4f spectra acquired from the Au-rich NPs (Cu₇₅Au₂₅) after H₂ annealing treatment predominantly exhibit the alloy Au state with a BE of 84.5 eV (Figure 1(a)). This observation indicates that the Au-rich NPs exhibit a less tendency of Au surface segregation compared to Au-poor NPs. This difference is evidenced by the lower intensity of the pure Au peak and negligible intensity changes in both the Au 4f and Cu 3p spectra during H₂ annealing and after the complete reduction of surface Cu oxides. Therefore, Au atoms in the Aurich NPs maintain the alloy state, where the adequate amount of Au allows for maximizing Cu-Au pairwise interactions across both the surface and bulk regions, thereby lowering the driving force for Au surface segregation. Conversely, the deficiency of Au in Au-poor NPs provides a stronger driving force for Au surface segregation to release the lattice strain in the bulk (due to the larger atom size of Au than Cu). Since Au possesses smaller surface energy than Cu, the subsequent clustering of segregated Au atoms leads to the lowered surface energy of the NPs. Consequently, the Au-poor NPs undergo phase separation via surface segregation and subsequent clustering of Au atoms. Figures 4(a, c) schematically illustrate the contrasting outcomes of H2 annealing treatment, showing that the surface region of Au-poor NPs is decorated by embedded Au clusters, whereas the Au-rich NPs transform into an Au-enriched shell structure while preserving the alloy Au state throughout both the surface and bulk regions.

By contrast, the Au 4f spectra acquired from the Au-rich NPs (Cu₇₅Au₂₅) after H₂ annealing treatment predominantly exhibit the alloy Au state with a BE of 84.5 eV (Figure 1(a)). This observation indicates that the Au-rich NPs exhibit a less tendency of Au surface segregation compared to Au-poor NPs. This difference is evidenced by the lower intensity of the pure Au peak and negligible intensity changes in both the Au 4f and Cu 3p spectra during H₂ annealing and after the complete reduction of surface Cu oxides. Therefore, Au atoms in the Aurich NPs maintain the alloy state, where the adequate amount of Au allows for maximizing Cu-Au pairwise interactions across both the surface and bulk regions, thereby lowering the driving force for Au surface segregation. Conversely, the deficiency of Au in Au-poor NPs provides a stronger driving force for Au surface segregation to release the lattice strain in the bulk (due to the larger atom size of Au than Cu). Since Au possesses smaller surface energy than Cu, the subsequent clustering of segregated Au atoms leads to the lowered surface energy of the NPs. Consequently, the Au-poor NPs undergo phase separation via surface segregation and subsequent clustering of Au atoms. Figures 4(a, c) schematically illustrate the contrasting outcomes of H₂ annealing treatment, showing that the surface region of Au-poor NPs is decorated by embedded Au clusters, whereas the Au-rich NPs transform into an Au-enriched shell structure while preserving the alloy Au state throughout both the surface and bulk regions. Figures 4(b, d) depict the outcomes following O_2 annealing treatment. For the Au-poor NPs, the surfaces retain embedded Au clusters that are still active for catalytic reactions. Conversely, the Aurich NPs develop a complete CuO shell on their surfaces.

The AP-XPS experiment and DFT modeling findings are further supported by ex-situ scanning transmission electron microscopy (STEM) imaging of $Cu_{75}Au_{25}$ and $Cu_{90}Au_{10}$ NPs following H_2 and O_2 annealing treatments. In Figure 4(e), high-angle annular dark-field (HAADF) STEM imaging of an H_2 -treated $Cu_{90}Au_{10}$ NP reveals the presence of small Au clusters embedded within the surface region of the NP, instead

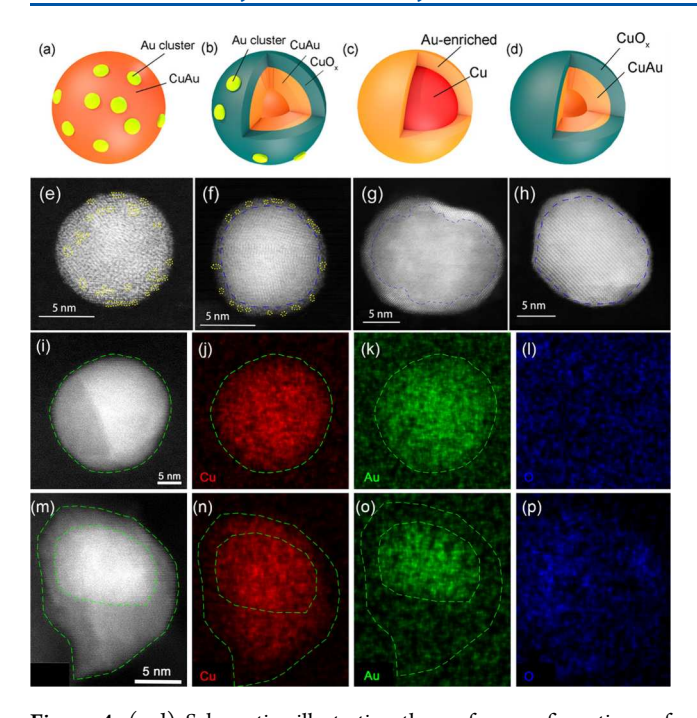


Figure 4. (a-d) Schematics illustrating the surface configurations of Cu-Au NPs under H₂ and O₂ atmospheres. (a) Formation of Au clusters embedded in the surface region of Au-poor NPs (Cu₉₀Au₁₀) during H₂ annealing, and (b) their oxidation into a core-shell configuration composed of a CuAu core and a partial CuO shell with embedded Au clusters when subjected to an O2 atmosphere. (c) Formation of an Au-enriched shell while preserving the alloy Au state throughout both the surface and bulk regions for Au-rich NPs (Cu₇₅Au₂₅) during H₂ annealing, and (d) their oxidation into a coreshell structure consisting of a CuAu core and a complete CuO shell, when exposed to an O2 atmosphere. (e-h) STEM HAADF images of oxidized Cu₉₀Au₁₀ and Cu₇₅Au₂₅ NPs. In (e), yellow dotted circles indicate embedded Au clusters in the surface region of an H₂annealed Cu₉₀Au₁₀ NP. In (f), the blue dashed line denotes the CuO_x shell with weaker image intensity, while yellow dotted circles highlight Au clusters embedded in the CuO_x shell of an O₂-annealed Cu₉₀Au₁₀ NP. In (g), the dashed line roughly delineates the boundary between the Au-enriched shell and Au-depleted core of an H₂-annealed Cu₇₅Au₂₅ NP. In (h), the dashed line marks the CuO_x shell (exhibiting weaker image intensity) of an O₂-annealed Cu₇₅Au₂₅ NP. (i-p) STEM HAADF images and corresponding STEM-EDS maps of Cu, Au and O of $Cu_{90}Au_{10}$ and $Cu_{75}Au_{25}$ NPs. The green dashed lines highlight the core-shell feature associated with Au enrichment in the core region for the Cu₇₅Au₂₅ NP, while indicating the absence of such a core-shell configuration in the Au distribution for the Cu₉₀Au₁₀ NP. The NPs in (f, h, i, m) were subjected to H₂ annealing at 400 °C in 1 \times 10⁻³ Torr H₂, followed by annealing in 1 \times 10⁻³ Torr O₂ at 400 °C.

of a CuAu alloy shell. Figure 4(f) shows a HAADF-STEM image of the $Cu_{90}Au_{10}$ NP after O_2 annealing treatment, where embedded Au clusters appear as atom columns with stronger image intensity within a formed CuO_x shell. Figures 4(g) and 4(h) present HAADF images of $Cu_{75}Au_{25}$ NPs following H_2 and O_2 treatments, respectively. Figure 4(g) reveals stronger image intensities from the shell region compared to the bulk region of an H_2 -treated $Cu_{75}Au_{25}$ NP, indicating surface segregation of Au and consequent Au enrichment in the shell. Figure 4(h) shows the formation of a continuous CuO_x shell on the $Cu_{75}Au_{25}$ NP after O_2 annealing, illustrating a contrasting behavior compared with the $Cu_{90}Au_{10}$ NP.

This difference in the Au distribution between the Cu90Au10 and Cu75Au25 NPs is further elucidated by

STEM-EDS mapping. Figures 4(i-l) present a STEM-HAADF image and corresponding STEM-EDS elemental maps of an oxidized Cu90Au10 NP. Although the spatial resolution of the EDS mapping is insufficient to resolve individual Au clusters of ~0.5 nm in the outermost surface region (as noted in Figure 4(f)), the relatively uniform intensity across the entire NP in both the Cu and Au maps suggests the presence of Au clusters in the surface region of the NP. In contrast, Figures 4(m-p) display a STEM-HAADF image and STEM-EDS elemental maps of a Cu75Au25 NP oxidized under the same condition as the Cu₉₀Au₁₀ NP. The Cu₇₅Au₂₅ NP exhibits a relatively uniform distribution of Cu, while Au is highly concentrated in the core region. This contrast indicates a more spread presence of Au throughout the entire Cu₉₀Au₁₀ NP, compared to the significant enrichment of Au in the core region of the Cu75Au25 NP. Additionally, the uniform and weak intensity in the O maps for both NPs indicates the ultrathin nature of the oxide shell.

Alloying represents a compelling strategy for enhancing catalytic properties, surpassing those attainable with pure metals. However, a significant knowledge gap persists regarding the dynamic interplay between alloy composition and surface segregation under reaction conditions. As shown above, our results demonstrate that Au-poor NPs tend to undergo phase separation in H2 atmospheres, leading to the emergence of Au nanoclusters at the surface. In O₂ atmospheres, these Au clusters impede the formation of a complete oxide shell. By contrast, Au-rich NPs maintain their alloy state without obvious phase separation in H₂ atmospheres. This in turn results in uniform oxide growth on the NPs and the formation of a complete oxide shell in O₂ atmospheres. Cu-Au NPs serve as catalysts for a wide variety of catalytic oxidation reactions such as CO oxidation,³² methanol oxidation,³⁵ steaming reforming,³⁶ and the water-gas-shift reactions.³⁷ In these chemical processes, a critical concern is the surface oxidation of Cu, which can significantly impact the catalytic performance of Cu-based catalysts. 38,39 As discussed above, the oxidation of Au-Cu NPs results in the formation of mixed Au nanoclusters and CuO on the surface in the case of Au-poor NPs, whereas Au-rich NPs develop into a complete CuO shell. These distinctions in oxide formation and surface configuration offer opportunities to fine-tune the reactivity and selectivity of Cu-Au catalysts. Figure 5 illustrates the CO conversion rates during CO oxidation catalyzed by Cu75Au25 and Cu90Au10 NPs, respectively, subjected to different treatments. For the Cu₇₅Au₂₅ NPs, the CO conversion rate initially remains low, starting to increase around 200 °C. Cu₇₅Au₂₅ NPs treated with O₂ for 1 h exhibit the slowest increase in CO conversion due to the formation of CuO on the surface, which reduces catalytic activity. H₂treated and fresh Cu₇₅Au₂₅ NPs show a faster increase in CO conversion, but their catalytic activity declines around 350 °C due to CuO formation on the surface. In contrast, for the Cu₉₀Au₁₀ NPs, the initial CO conversion rate is similarly low, beginning to rise at around 300 °C. This delay is attributed to the lower Au content in Cu₉₀Au₁₀, resulting in fewer active Au sites on the surface. However, the CO conversion of H_2 -treated Cu₉₀Au₁₀ NPs continues to increase up to 400 °C, unlike fresh or O_2 treated $Cu_{90}Au_{10}$ NPs and $H_2\text{-treated}$ $Cu_{75}Au_{25}$ NPs. This persistence in activity is attributed to the presence of residual Au clusters embedded in the NP surface, which retain active Au sites and align well with XPS measurements on the surface stability of Au clusters.

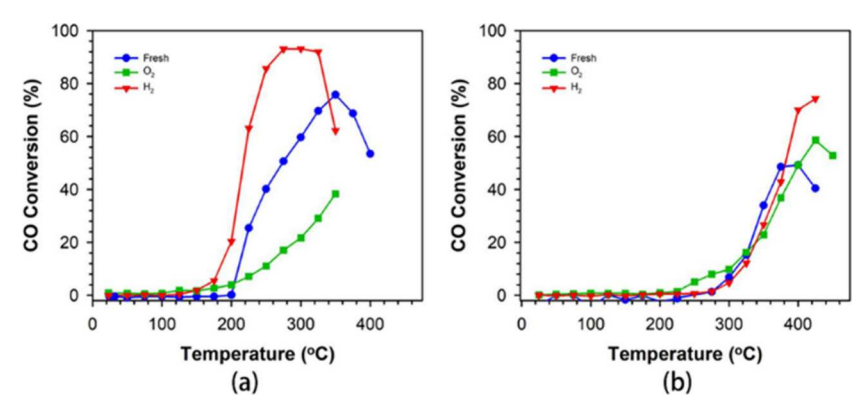


Figure 5. CO conversion during the CO + O_2 reaction as a function of temperature for samples of (a) $Cu_{75}Au_{25}$ and (b) $Cu_{90}Au_{10}$ NPs: (blue) fresh, (red) H_2 -treated (15 vol % H_2 , 400 °C, 1 h), (green) O_2 -treated (20 vol % O_2 . 260 °C, 1 h).

It is also noted from Figure 5 that the O_2 -treated $Cu_{75}Au_{25}$ sample exhibits higher CO oxidation activity compared to the O₂-Cu₉₀Au₁₀ sample at 350 °C. This difference can be attributed to the O2 treatment conditions. Both samples were initially treated with O₂ at 260 °C, which is lower than the 400 °C used in the AP-XPS measurements. The Cu₇₅Au₂₅ sample, with its higher Au content, is more resistant to oxidation, resulting in incomplete oxidation and a substantial amount of residual Au clusters within the CuO_x shell. In contrast, the Cu₉₀Au₁₀ sample undergoes more extensive oxidation, leading to a greater surface oxide content and fewer Au clusters within the CuO_x shell. Consequently, the Cu₇₅Au₂₅ sample shows enhanced CO oxidation activity at ~350 °C due to the catalytic enhancement effect of the higher concentration of Au clusters. However, at 400 °C, the Cu₉₀Au₁₀ sample demonstrates superior CO oxidation activity, which is attributed to the high stability of Au clusters within the CuO_x shell. This observation is consistent with the AP-XPS measurements performed at 400 °C, which indicate that Cu₇₅Au₂₅ NPs fully oxidize into a complete CuO_x shell, whereas the Cu₉₀Au₁₀ NPs retain stable Au clusters within the CuO_x shell, contributing to their enhanced CO oxidation performance.

It is also crucial to consider the impact of NP size effects on the observed difference in CO oxidation activity between the Au-rich and Au-poor samples, as illustrated in Figure 5. Key effects include: (i) initial particle size distribution of assynthesized NPs-smaller NPs generally offer a higher surface area and more active Au species for the reaction; (ii) dynamic evolution of NP sizes during catalysis - NPs tend to coarsen, with smaller NPs aggregating onto larger ones-this process reduces the overall number of Au species available on the NP surfaces; and (iii) effect of alloy composition on coarsening behavior-variations in Au/Cu ratios may influence the strength of metal-metal interactions and the propensity of NPs to coarsen. These size effects interact with the distribution and stability of Au clusters within the CuO_x shell. NPs that coarsen more rapidly may develop fewer Au clusters, potentially increasing their susceptibility to deactivation at elevated temperatures. Therefore, a thorough understanding of how coarsening behavior varies with alloy composition is essential. This knowledge will help differentiate between the effects of active Au abundance and the intrinsic activity of the NPs

Au sites surrounded by Cu or Cu oxides can indeed contribute to high catalytic activity. 6,40 However, oxidation can

lead to the formation of an oxide shell that can block these Au sites, thereby reducing catalytic activity, especially in Au-rich NPs. Conversely, Au nanoclusters formed during H₂ pretreatment of Au-poor NPs can expose more Au sites on the oxidized surface. Consequently, the catalytic activity of H₂treated catalyst with low Au composition may be more advantageous than those with higher bulk Au composition under certain conditions, due to increased exposure of Au clusters and their enhanced surface stability during reactions. Moreover, smaller clusters often exhibit more of the lesscoordinated sites, such as corners and edges, which can exhibit specific activity and improved selectivity. The insights in this work provide a foundation for the development of more efficient and selective catalytic materials, offering promising avenues for future research in catalysis design and optimization.

In summary, our investigation sheds light on the dynamic surface segregation and oxidation behavior of Cu-Au NPs with varying compositions. Through in-depth analysis employing AP-XPS, TEM, and DFT calculations, we uncover the formation of Au nanoclusters in the surface region of Au-poor NPs during H_2 treatment, a phenomenon that persists upon O_2 exposure. By contrast, Au-rich NPs undergo transformation into an Au-enriched shell in an H2 atmosphere, which subsequently oxidizes into a complete CuO_x shell when subjected to O2. This dynamic behavior highlights the unexpected outcome of lowering the bulk Au composition in preserving the precious noble metal at the surface, with potentially significant implications for tailoring the surface properties of bimetallic NPs to enhance catalytic performance. Furthermore, our findings offer insights for the design and optimization of catalyst materials, opening avenues for the development of more efficient and selective catalytic systems across various chemical processes.

■ MATERIALS AND METHODS

Chemicals. Copper(II) chloride dihydrate (CuCl₂·2H₂O 99% pure) was obtained from Lancaster Synthesis, while hydrogen tetrachloroaurate (III) hydrate (HAuCl4) was sourced from Strem Chemicals. Tetra-*n*-octylammonium bromide (TOABr, 98%) was procured fromAlfa Aesar. 1–Decanethiol (96%), potassium bromide (99%), sodium borohydride (99%), hexane, toluene, and other commonly used solvents were acquired from Aldrich. Water was purified using a Millipore Direct-Q system, achieving a final resistance of 18.2 M Ohm. HOPG was obtained from SPI Supplies.

Synthesis of Cu- and Au-Precursor Nanoparticles. The synthesis of decanethiolate (DT) capped Au nanoparticles followed a modified two-phase reduction method. ^{12,41,42} The synthesis of decanethiolatecapped Cu nanoclusters was carried out as previously described. ^{12,43} In brief, CuCl₂ was dissolved in water in the presence of 4.3 M KBr. Cu²⁺ was converted to CuBr₄²⁻, which was subsequently transferred from the aqueous phase to the organic phase by adding a solution of TOABr in toluene (40 mL toluene, 180 mM TOABr). After 20 min of vigorous stirring, the aqueous solution was removed, and the toluene solution was stirred under argon purge to eliminate oxygen from the system. Then, 0.36 mL of decanethiol was added, and the solution was stirred for an additional hour, resulting in a color change from from dark purple to light green. A solution of NaBH₄ (25 mL, 0.4 M) was added

Synthesis of AuCu Alloy Nanoparticles from Mixed Cu- and Au-Precursor Nanoparticles. The solutions of the as-synthesized Au and Cu nanoparticles were mixed in a controlled ratio. This mixed solution was then concentrated by a factor of ~15 in a glass reactor and maintained in an oven under controlled temperature conditions and reaction time. Through experimentation across a range of temperature from 150 to 170 °C, 156 °C was identified as the optimal temperature for forming nanocubes.

dropwise. After reaction for 2 h under argon, the aqueous layer was removed, and the solution was stirred overnight.

Ambient-Pressure X-ray Photoelectron Spectroscopy. AP-XPS experiments were performed at the IOS beamline of the National Synchrotron Light Source II (NSLS-II), Brookhaven National Laboratory. The AP-XPS instrument is equipped with a reaction chamber with the base pressure $<5 \times$ 10⁻⁹ Torr, a SPECS Phoibos NAP150 hemispherical analyzer, and a sputtering gun for surface preparation. The multiple differential pumping stages between the reaction chamber and the hemispherical analyzer create a pressure difference by maintaining ultrahigh vacuum conditions (lower than 1×10^{-7} Torr) in the analyzer while the pressure in the reaction chamber is a few Torr. Photoemitted electrons leave the highpressure reaction chamber through a small cone-shaped aperture into the differentially pumped transfer lenses system toward the electron energy analyzer, thereby allowing for continuously acquiring XPS spectra at pressures of up to ~5 Torr in the reaction chamber. The photon energy used was 650 eV for Au 4f, Cu 3p, and 1150 eV for Cu LMM relevant for the present work. Scofield sensitive factors are introduced into the integrated peak areas of each species in the same binding energy region in order to calculate the relative composition evolution in the corresponding detection depth.

Transmission Electron Microscopy. HAADF-STEM observations and elemental mapping of Cu–Au NPs after $\rm H_2$ and $\rm O_2$ treatments were performed with FEI Talos F200X microscopy operated at 200 kV.

Catalytic Activity Measurement. The catalytic activity of the catalysts for CO (1 vol % balanced by N_2) + O_2 (20 vol % balanced by N_2) reaction was measured using a customer-built system including a temperature-controlled reactor, gas flow/mixing/injection controllers, and an online gas chromatograph (Shimadzu GC 8A) equipped with 5A molecular sieve and Porapak Q packed columns and a thermal conductivity detector. The catalytic activity for CO oxidation was determined by analyzing the composition of the tail gas

effusing from the quartz microreactor packed with catalyst fixed bed.

Density Functional Theory (DFT) Modeling. Periodic DFT calculations were performed using the Vienna Ab initio Simulation Package (VASP). 44-46 Perdew, Burke, and Ernzerhof (PBE) generalized gradient approximation (GGA) and the projector augmented-wave (PAW) potentials were used to describe the electron–electron exchange and core–electron potential separately. The plane-wave cutoff energy was set to be 500 eV. The Brillouin-zone integration was performed using (4 × 4 × 1) K-point meshes based on Monkhorst–Pack grids. Core-level electron-binding energies were calculated using the transition-state model of the excited systems.

ASSOCIATED CONTENT

Solution Supporting Information

The Supporting Information is available free of charge at https://pubs.acs.org/doi/10.1021/acs.jpclett.4c02172.

Evolution of Au 4f and Cu 3p spectra acquired during H_2 annealing of Cu, $Cu_{50}Au_{50}$ and $Cu_{95}Au_5$ NPs (Figure S1) and during O_2 annealing of H_2 -treated $Cu_{50}Au_{50}$ and $Cu_{95}Au_5$ NPs (Figure S2) (PDF)

AUTHOR INFORMATION

Corresponding Author

Guangwen Zhou — Department of Mechanical Engineering and Materials Science and Engineering Program, State University of New York at Binghamton, Binghamton, New York 13902, United States; ⊙ orcid.org/0000-0002-9243-293X; Email: gzhou@binghamton.edu

Authors

Jianyu Wang — Department of Mechanical Engineering and Materials Science and Engineering Program, State University of New York at Binghamton, Binghamton, New York 13902, United States

Xiaobo Chen — Department of Mechanical Engineering and Materials Science and Engineering Program, State University of New York at Binghamton, Binghamton, New York 13902, United States

Chaoran Li — Department of Mechanical Engineering and Materials Science and Engineering Program, State University of New York at Binghamton, Binghamton, New York 13902, United States

Yaguang Zhu — Department of Mechanical Engineering and Materials Science and Engineering Program, State University of New York at Binghamton, Binghamton, New York 13902, United States

Jing Li – Materials Science and Engineering Program and Department of Chemistry, State University of New York at Binghamton, Binghamton, New York 13902, United States

Shiyao Shan — Materials Science and Engineering Program and Department of Chemistry, State University of New York at Binghamton, Binghamton, New York 13902, United States; orcid.org/0000-0001-9240-7227

Yupeng Wu — Department of Mechanical Engineering and Materials Science and Engineering Program, State University of New York at Binghamton, Binghamton, New York 13902, United States

- Adrian Hunt National Synchrotron Light Source II, Brookhaven National Laboratory, Upton, New York 11973, United States; orcid.org/0000-0002-5283-9647
- Iradwikanari Waluyo National Synchrotron Light Source II, Brookhaven National Laboratory, Upton, New York 11973, United States; orcid.org/0000-0002-4046-9722
- J. Anibal Boscoboinik Center for Functional Nanomaterials, Brookhaven National Laboratory, Upton, New York 11973, United States; Occid.org/0000-0002-5090-7079
- Xiao Tong Center for Functional Nanomaterials, Brookhaven National Laboratory, Upton, New York 11973, United States
- Chuan-Jian Zhong Materials Science and Engineering Program and Department of Chemistry, State University of New York at Binghamton, Binghamton, New York 13902, United States; Oorcid.org/0000-0003-0746-250X

Complete contact information is available at: https://pubs.acs.org/10.1021/acs.jpclett.4c02172

Author Contributions

The manuscript was written through contributions of all authors. All authors have given approval to the final version of the manuscript.

Notes

The authors declare no competing financial interest.

ACKNOWLEDGMENTS

This work was supported by the U.S. Department of Energy (DOE), Office of Basic Energy Sciences, Division of Materials Sciences and Engineering under Award No. DE-SC0001135. The work on the synthesis and preparation of the nanoparticles and catalysts was supported by the National Science Foundation (CHE 2102482). This research used the 23-ID-2 (IOS) beamline at the National Synchrotron Light Source II, the Electron Microcopy Facilities and the Theory and Computation resources of the Center for Functional Nanomaterials, which are U.S. DOE Office of Science User Facilities, at Brookhaven National Laboratory under Contract No. DE-SC0012704.

REFERENCES

- (1) Allison, E. G.; Bond, G. C. The Structure and Catalytic Properties of Palladium-Silver and Palladium-Gold Alloys. *Catalysis Reviews* **1972**, 7 (2), 233–289.
- (2) Hashimoto, K. Recent Advances in the Catalytic Properties of Metastable Materials. *Materials Science and Engineering: A* **1997**, 226–228, 891–899.
- (3) Shan, S.; Luo, J.; Yang, L.; Zhong, C.-J. Nanoalloy Catalysts: Structural and Catalytic Properties. *Catal. Sci. Technol.* **2014**, *4* (10), 3570–3588.
- (4) Ou, T.-C.; Chang, F.-W.; Roselin, L. S. Production of Hydrogen via Partial Oxidation of Methanol over Bimetallic Au-Cu/TiO₂ Catalysts. *J. Mol. Catal. A: Chem.* **2008**, 293 (1), 8–16.
- (5) Yin, A.; Wen, C.; Dai, W.-L.; Fan, K. Nanocasting of CuAu Alloy Nanoparticles for Methyl Glycolate Synthesis. *J. Mater. Chem.* **2011**, 21 (25), 8997–8999.
- (6) Yin, J.; Shan, S.; Yang, L.; Mott, D.; Malis, O.; Petkov, V.; Cai, F.; Shan Ng, M.; Luo, J.; Chen, B. H.; Engelhard, M.; Zhong, C.-J. Gold-Copper Nanoparticles: Nanostructural Evolution and Bifunctional Catalytic Sites. *Chem. Mater.* **2012**, 24 (24), 4662–4674.
- (7) Kim, D.; Resasco, J.; Yu, Y.; Asiri, A. M.; Yang, P. Synergistic Geometric and Electronic Effects for Electrochemical Reduction of Carbon Dioxide Using Gold-Copper Bimetallic Nanoparticles. *Nat. Commun.* **2014**, 5 (1), 4948.

- (8) Liu, K.; Zhang, S.; Wu, D.; Luo, L.; Sun, X.; Chen, X.; Zakharov, D.; Cheng, S.; Zhu, Y.; Yang, J. C.; Wang, G.; Zhou, G. Effect of Surface Steps on Chemical Ordering in the Subsurface of Cu(Au) Solid Solutions. *Phys. Rev. B* **2021**, *103* (3), 035401.
- (9) Zou, L.; Yang, C.; Lei, Y.; Zakharov, D.; Wiezorek, J. M. K.; Su, D.; Yin, Q.; Li, J.; Liu, Z.; Stach, E. A.; Yang, J. C.; Qi, L.; Wang, G.; Zhou, G. Dislocation Nucleation Facilitated by Atomic Segregation. *Nat. Mater.* **2018**, *17* (1), 56–63.
- (10) Li, C.; Liu, Q.; Boscoboinik, J. A.; Zhou, G. Tuning the Surface Composition of Cu₃Au Binary Alloy. *Phys. Chem. Chem. Phys.* **2020**, 22 (6), 3379–3389.
- (11) Zhu, Y.; Wu, D.; Li, C.; Tong, X.; Boscoboinik, J. A.; Sadowski, J. T.; Zhou, G. Atomistic Mechanisms of the Initial Oxidation of Stepped Cu₃Au(100). *Phys. Rev. B* **2022**, *105* (7), 075422.
- (12) Sachtler, W. M. H.; van Santen, R. A. Surface Composition of Binary Alloys. *Applications of Surface Science* **1979**, 3 (2), 121–144.
- (13) Sinfelt, J. H. Catalysis by Alloys and Bimetallic Clusters. Acc. Chem. Res. 1977, 10 (1), 15–20.
- (14) Wang, J.; Li, C.; Zhu, Y.; Boscoboinik, J. A.; Zhou, G. Insight into the Phase Transformation Pathways of Copper Oxidation: From Oxygen Chemisorption on the Clean Surface to Multilayer Bulk Oxide Growth. *J. Phys. Chem. C* **2018**, *122* (46), 26519–26527.
- (15) Li, C.; Liu, Q.; Boscoboinik, J. A.; Zhou, G. Tuning the Surface Composition of Cu₃Au Binary Alloy. *Phys. Chem. Chem. Phys.* **2020**, 22 (6), 3379–3389.
- (16) Ozawa, K.; Oba, Y.; Edamoto, K. Formation and Characterization of the Cu₂O Overlayer on Zn-Terminated ZnO(0001). *Surf. Sci.* **2009**, *603* (13), 2163–2170.
- (17) Yi, C.-W.; Luo, K.; Wei, T.; Goodman, D. W. The Composition and Structure of Pd-Au Surfaces. *J. Phys. Chem. B* **2005**, *109* (39), 18535–18540.
- (18) Peters, S.; Peredkov, S.; Neeb, M.; Eberhardt, W.; Al-Hada, M. Size-Dependent XPS Spectra of Small Supported Au-Clusters. *Surf. Sci.* **2013**, *608*, 129–134.
- (19) Radnik, J.; Mohr, C.; Claus, P. On the Origin of Binding Energy Shifts of Core Levels of Supported Gold Nanoparticles and Dependence of Pretreatment and Material Synthesis. *Phys. Chem. Chem. Phys.* **2003**, *5* (1), 172–177.
- (20) Bukhtiyarov, A. V.; Prosvirin, I. P.; Bukhtiyarov, V. I. XPS/STM Study of Model Bimetallic Pd-Au/HOPG Catalysts. *Appl. Surf. Sci.* **2016**, *367*, 214–221.
- (21) Kalinkin, A. V.; Smirnov, M. Yu.; Bukhtiyarov, A. V.; Bukhtiyarov, V. I. XPS Study of Gold Oxidation with Nitrogen Dioxide in Model Au/C Samples. *Kinet. Catal* **2015**, *56* (6), 796–800. (22) Sun, C. Q.; Pan, L. K.; Fu, Y. Q.; Tay, B. K.; Li, S. Size Dependence of the 2p-Level Shift of Nanosolid Silicon. *J. Phys. Chem. B* **2003**, *107* (22), 5113–5115.
- (23) Vogel, M.; Kasigkeit, C.; Hirsch, K.; Langenberg, A.; Rittmann, J.; Zamudio-Bayer, V.; Kulesza, A.; Mitrić, R.; Möller, T.; Issendorff, B.; Lau, J. T. 2p Core-Level Binding Energies of Size-Selected Free Silicon Clusters: Chemical Shifts and Cluster Structure. *Phys. Rev. B* **2012**, *85* (19), 195454.
- (24) Dalacu, D.; Klemberg-Sapieha, J. E.; Martinu, L. Substrate and Morphology Effects on Photoemission from Core-Levels in Gold Clusters. *Surf. Sci.* **2001**, 472 (1), 33–40.
- (25) Büttner, M.; Oelhafen, P. XPS Study on the Evaporation of Gold Submonolayers on Carbon Surfaces. *Surf. Sci.* **2006**, *600* (5), 1170–1177.
- (26) Richter, B.; Kuhlenbeck, H.; Freund, H.-J.; Bagus, P. S. Cluster Core-Level Binding-Energy Shifts: The Role of Lattice Strain. *Phys. Rev. Lett.* **2004**, 93 (2), 026805.
- (27) Anderson, D. P.; Alvino, J. F.; Gentleman, A.; Qahtani, H. A.; Thomsen, L.; Polson, M. I. J.; Metha, G. F.; Golovko, V. B.; Andersson, G. G. Chemically-Synthesised, Atomically-Precise Gold Clusters Deposited and Activated on Titania. *Phys. Chem. Chem. Phys.* **2013**, *15* (11), 3917–3929.
- (28) Wu, Y.; Garfunkel, E.; Madey, T. E. Initial Stages of Cu Growth on Ordered Al₂O₃ Ultrathin Films. *Journal of Vacuum Science & Technology A* **1996**, *14* (3), 1662–1667.

- (29) Bagus, P. S.; Wieckowski, A.; Freund, H. Initial and Final State Contributions to Binding-Energy Shifts Due to Lattice Strain: Validation of Auger Parameter Analyses. *Chem. Phys. Lett.* **2006**, 420 (1), 42–46.
- (30) Cavicchi, R. E.; Silsbee, R. H. Dynamics of Tunneling to and from Small Metal Particles. *Phys. Rev. B* **1988**, *37* (2), 706–719.
- (31) Sengar, S. K.; Mehta, B. R.; Govind. Size and Alloying Induced Shift in Core and Valence Bands of Pd-Ag and Pd-Cu Nanoparticles. *J. Appl. Phys.* **2014**, *115* (12), 124301.
- (32) Pueyo Bellafont, N.; Bagus, P. S.; Illas, F. Prediction of Core Level Binding Energies in Density Functional Theory: Rigorous Definition of Initial and Final State Contributions and Implications on the Physical Meaning of Kohn-Sham Energies. *J. Chem. Phys.* 2015, 142 (21), 214102.
- (33) Phala, N. S.; Klatt, G.; van Steen, E. A DFT Study of Hydrogen and Carbon Monoxide Chemisorption onto Small Gold Clusters. *Chem. Phys. Lett.* **2004**, 395 (1-3), 33–37.
- (34) Huang, T.-J.; Tsai, D.-H. CO Oxidation Behavior of Copper and Copper Oxides. Catal. Lett. 2003, 87 (3), 173–178.
- (35) Ammon, Ch.; Bayer, A.; Held, G.; Richter, B.; Schmidt, Th.; Steinrück, H.-P. Dissociation and Oxidation of Methanol on Cu(110). *Surf. Sci.* **2002**, *507*–*510*, 845–850.
- (36) Peppley, B. A.; Amphlett, J. C.; Kearns, L. M.; Mann, R. F. Methanol-Steam Reforming on Cu/ZnO/Al₂O₃. Part 1: The Reaction Network. *Applied Catalysis A: General* **1999**, *179* (1), 21–29.
- (37) Gokhale, A. A.; Dumesic, J. A.; Mavrikakis, M. On the Mechanism of Low-Temperature Water Gas Shift Reaction on Copper. J. Am. Chem. Soc. 2008, 130 (4), 1402–1414.
- (38) Vivek, S.; Preethi, S.; Kumar, T. H. V.; Sundramoorthy, A. K.; Babu, K. S. Oxidation Studies on Mono (Cu, Ni) and Bimetallic (Cu-Ni) Nanoparticles and Its Impact on Catalytic Activity. *J. Alloys Compd.* **2020**, *816*, 152608.
- (39) Iwamoto, H.; Kameoka, S.; Xu, Y.; Nishimura, C.; Tsai, A. P. Effects of Cu Oxidation States on the Catalysis of NO+CO and N₂O +CO Reactions. *J. Phys. Chem. Solids* **2019**, *125*, 64–73.
- (40) Qi, C.; Zheng, Y.; Lin, H.; Su, H.; Sun, X.; Sun, L. CO Oxidation over Gold Catalysts Supported on CuO/Cu₂O Both in O₂-Rich and H₂-Rich Streams: Necessity of Copper Oxide. *Applied Catalysis B: Environmental* **2019**, 253, 160–169.
- (41) Brust, M.; Walker, M.; Bethell, D.; Schiffrin, D. J.; Whyman, R. Synthesis of Thiol-Derivatised Gold Nanoparticles in a Two-Phase Liquid-Liquid System. *J. Chem. Soc., Chem. Commun.* **1994**, 0 (7), 801–802
- (42) Hostetler, M. J.; Zhong, C.-J.; Yen, B. K. H.; Anderegg, J.; Gross, S. M.; Evans, N. D.; Porter, M.; Murray, R. W. Stable, Monolayer-Protected Metal Alloy Clusters. *J. Am. Chem. Soc.* **1998**, 120 (36), 9396–9397.
- (43) Mott, D.; Galkowski, J.; Wang, L.; Luo, J.; Zhong, C.-J. Synthesis of Size-Controlled and Shaped Copper Nanoparticles. *Langmuir* **2007**, 23 (10), 5740–5745.
- (44) Kresse, G.; Furthmüller, J. Efficient Iterative Schemes for Ab Initio Total-Energy Calculations Using a Plane-Wave Basis Set. *Phys. Rev. B* **1996**, *54* (16), 11169–11186.
- (45) Kresse, G.; Furthmüller, J. Efficiency of Ab-Initio Total Energy Calculations for Metals and Semiconductors Using a Plane-Wave Basis Set. *Comput. Mater. Sci.* **1996**, *6* (1), 15–50.
- (46) Kresse, G.; Furthmüller, J. Efficient Iterative Schemes for Ab Initio Total-Energy Calculations Using a Plane-Wave Basis Set. *Phys. Rev. B* **1996**, *54* (16), 11169–11186.
- (47) Perdew, J. P.; Burke, K.; Ernzerhof, M. Generalized Gradient Approximation Made Simple. *Phys. Rev. Lett.* **1996**, 77 (18), 3865–3868.
- (48) Monkhorst, H. J.; Pack, J. D. Special Points for Brillouin-Zone Integrations. *Phys. Rev. B* **1976**, 13 (12), 5188–5192.
- (49) Göransson, C.; Olovsson, W.; Abrikosov, I. A. Numerical Investigation of the Validity of the Slater-Janak Transition-State Model in Metallic Systems. *Phys. Rev. B* **2005**, 72 (13), 134203.